

## TERSat: Trapped Energetic Radiation Satellite

Emily Clements, Bruno Alvisio, Alessandra Babuscia, Zachary Casas, Brian Coffee, Sydney Giblin, Laura Hallock, Ryan Kingsbury, Michael Leaman, Naomi Lynch, Michael O'Connor, Elizabeth Qian, Frank Hall Schmidt, Maria de Soria-Santacruz, Lionel Sotomayor, Christian Valledor, Megan Tadge, Leonard Tampkins, Evan Wise, Mary Zhuang, Manuel Martinez-Sanchez, Kerri Cahoy

MIT Department of Aeronautics and Astronautics  
77 Massachusetts Ave.; (908) 216-7758  
egrosse@mit.edu

### ABSTRACT

Radiation damage caused by interactions with high-energy particles in the Van Allen Radiation Belts is a leading cause of component failures for satellites in low and medium Earth orbits (LEO, MEO). Very Low Frequency (VLF) electromagnetic waves have been shown to couple energy to high energy radiation belt particles and change their properties. For example, data from the IMAGE (Imager for Magnetopause-to-Aurora Global Exploration) satellite suggest that the gap between the inner and outer Van Allen belts is caused by lightning, which naturally generates VLF waves that scatter the pitch angle of high energy particles, such that they rejoin the neutral lower atmosphere.<sup>14</sup> It has been proposed that space-based antennas transmitting VLF waves could similarly help reduce the effects of radiation by scattering particles. However, the interaction between a VLF transmitter and the plasma environment is not sufficiently well understood, thus on-orbit experimentation and demonstration are needed to analyze how best to tune and couple VLF energy to the electrons and ions even though terrestrial VLF equipment is well understood and low-risk. TERSat is a 50 kg student-built nanosatellite that will analyze how VLF waves interact with the radiation environment at 550 km altitude by deploying two 2.5 m antennas to form a 5 m dipole, using a transmitter to radiate VLF waves over a range of voltage levels up to at least 600 V, frequencies from 3—50 kHz, and a range of magnetic field orientations. TERSat will also measure the strengths of the echoes with a VLF receiver. The spacecraft bus consists of a skinned isogrid structure, body-mounted solar cells for power generation, a reaction wheel attitude determination and control system (ADCS), and a customized student-built avionics board. TERSat is under development as part of the Air Force Research Laboratory (AFRL) University Nanosatellite Program 7 (UNP-7) competition. TERSat's science mission complements that of AFRL's Demonstration and Science Experiments (DSX) satellite. TERSat has the potential to occasionally interact and perform bistatic experiments with DSX, which will be in MEO, if both have overlapping operational periods. TERSat will support technology development of systems that can interact with and potentially reduce Van Allen Belt radiation by improving our understanding of transmitting and receiving VLF waves in a LEO satellite plasma environment.

### INTRODUCTION

The Trapped Energetic Radiation Satellite (TERSat) is a student-designed, nanosatellite (< 50 kg) that will investigate the ability of space-based Very Low Frequency (VLF) radio transmission to reduce the population of harmful high-energy particles in the inner Van Allen radiation belts. TERSat is MIT's entry into the AFRL University Nanosatellite Program (UNP) competition and receives support from UNP and NASA JPL. To date, TERSat has completed UNP-7's preliminary design review (PDR) and critical design review (CDR), and is building and testing an engineering development unit for proto-qualification review (PQR) and later the flight competition review (FCR).

TERSat will test the how effectively Very Low Frequency (VLF) waves can be radiated in LEO towards the goal of scattering trapped high energetic protons and electrons from the Van Allen Belts into the neutral atmosphere, thus reducing the hazardous effect of these particles on orbiting assets. High energy particles can become trapped in the Earth's magnetic field both due to natural causes such as cosmic rays and solar storms as well as adversarial actions. Increases in the level of high energy particles in the radiation belts pose a significant danger to both orbital assets and manned spaceflight. With few exceptions (such as natural events like lightning), electromagnetic energy at frequencies low enough to interact with electrons and ions is below the critical frequency of the Earth's ionosphere and thus cannot efficiently penetrate to

higher altitudes. Since ground-based efforts are thus ineffective, missions such as TERSat focus on testing the effectiveness of scattering electrons and ions in the radiation belts through the radiation of VLF waves on orbit. In particular, because TERSat will be in LEO, as the mission progresses and the orbit degrades, it will be capable of investigating transmission efficiency as a function of altitude as well as a function of frequency, power level, and orientation to the magnetic field.

TERSat is complementary to and designed to be compatible with the AFRL Demonstration and Science Experiment (DSX) satellite. TERSat will perform a subset of the DSX experiments at a much lower orbit, giving insight into the effects of altitude-dependent plasma density and magnetic field strength on the wave-particle interactions. TERSat is also capable of interacting with DSX for bistatic experiments if the mission periods overlap.

TERSat’s Mission Statements are shown in Table 1. To be successful, TERSat must accomplish both of the minimum success criteria: (i) transmit and characterize how effectively a VLF pulse is launched perpendicular to the local magnetic field, and (ii) receive VLF signals using an on-board receiver.

The main engineering goal of this project is to deploy two identical 2.5 m antennas, forming a 5 m dipole, that will investigate how effectively VLF waves can be launched and detected in the plasma environment of the Van Allen radiation Belts at a 550 km altitude. The TERSat transmitter will radiate VLF waves over a range of voltages, frequencies, and magnetic field orientations, and measure the strength of the echoes with a VLF receiver. It is important to note that this VLF transmit/receive experiment is entirely separate from TERSat’s S-band radio communication system.

**Table 1: Mission Statements and Success Criteria**

Statement	Description
MS1	<b>Objective Success Criteria:</b> Demonstrate and characterize transmission of low frequency (VLF) waves in the inner Van Allen radiation belt over a range of frequencies, over a range of voltages, and over a range of orientations to the magnetic field.
	<b>Minimum Success Criteria:</b> Demonstrate and characterize transmission of low frequency (VLF) waves in the inner Van Allen radiation belt near 50 kHz, at one voltage, with an orientation perpendicular to the magnetic field.
MS2	<b>Objective Success Criteria:</b> Demonstrate the ability to receive echoes/reflected signals resulting from transmitted pulses using an on-board VLF receiver.
	<b>Minimum Success Criteria:</b> Demonstrate the ability to receive VLF signals using an on-board VLF receiver.

The objective success criteria characterize the effects of frequency, voltage (power) and magnetic field orientation on how well VLF waves interact with electrons in plasma. TERSat will not only characterize how efficiently VLF waves can be radiated at LEO, but performing these experiments will also allow scientists to better calibrate underlying plasma physics models.

The minimum success criteria addresses a more basic but still critical science question: can a deployed antenna system overcome the antenna sheath impedance to radiate at VLF frequencies in the LEO plasma environment? Self-monitoring of the relative phase between the voltage and current on the transmitter should provide insight as to whether effective transmission occurs (if the voltage and current are in-phase, the system is well-matched). It is important to demonstrate the independent functionality of the VLF receiver by measuring other (natural or man-made) VLF signals in addition to any received self-echoes. For example, this would be useful if a reasonable match is measured at the transmitter and yet no self-echo is received.

**FLIGHT EXPERIMENT CONCEPT**

To accomplish the mission goals, the TERSat payload will deploy two 2.5 m Spiral Tube & Actuator for Controlled Extension/Retraction (STACER) antenna booms to create a dipole antenna, radiate VLF waves, and measure the strength of the echoes. The bus and deployed antennas are illustrated in Figure 1. TERSat’s baseline orbital altitude is 550 km, but altitudes up to 600 km will still satisfy the UNP de-orbit requirement<sup>2</sup> and are thus acceptable.

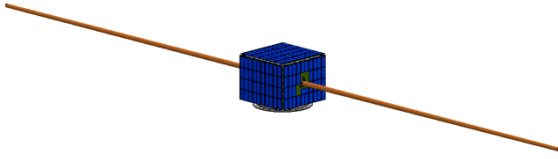


**Figure 1: TERSat with Deployed Antennas**

TERSat will radiate VLF waves at a variety of frequencies, voltages, and orientations to the magnetic field lines during the mission. The planned voltage levels are 100, 300, and 600 V, the planned frequencies are 3, 25, and 47 kHz, and the planned orientations are perpendicular, 45 degrees, and parallel to the magnetic field lines. The first experiments will be perpendicular to the magnetic field lines, working up in voltage to 600 V. The rationale for this approach is to still acquire useful experimental results even if the voltage at which there is arcing is much lower than expected.<sup>23</sup>

Figure 2 shows predicted radiated power levels as a function of frequency and orientation to the magnetic field for a 600 V input signal. The results in this figure are from a Matlab simulation, which is described in detail in the Payload Design section. For this scenario, optimal radiated power is predicted to be 32 W at a transmission frequency of 47 kHz and with an inductance of 0.3 H.

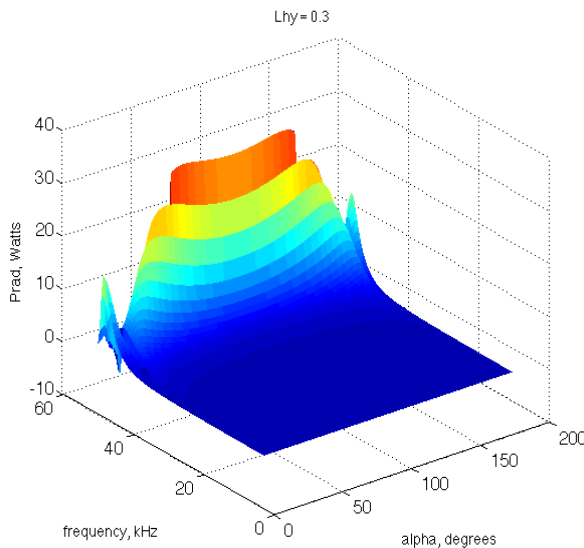


**Figure 2: Predicted Power Radiated for  $L = 0.3$  H and 600 V**

A possible addition to the experiment plan would be to interact with the AFRL satellite DSX. Such an interaction would add an additional dimension to the wave-particle interaction measurements. According to

Bortnik,<sup>6</sup> VLF waves not only travel and reflect along one magnetic field line, they also travel radially around and along other magnetic field lines. This would allow TERSat and DSX to monitor each other's transmissions and provide a better understanding of radial VLF wave propagation. This interaction is illustrated in Figure 3. The orange curve indicates the VLF wave's motion along the magnetic field lines. As noted by Bortnik<sup>8</sup>, the ability of a VLF wave to move radially has a dependence on transmitted frequency.

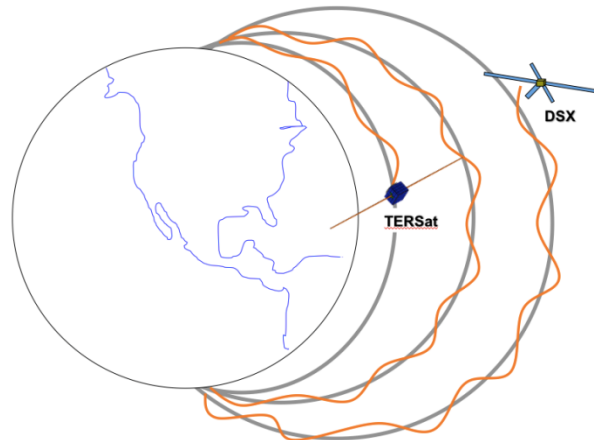


**Figure 3: TERSat Interaction with DSX**

Additionally, because plasma density and magnetic field strength varies with orbital parameters and altitude, TERSat could repeat DSX experiments to provide an understanding of how the density and field strength variations affect VLF propagation.

### SCIENCE BACKGROUND

The basic idea of radiation belt remediation methods is to promote precipitation of energetic particles via the scattering of their velocity direction into their loss cone. Charged particles execute a combination of rotation about and translation along the Earth's magnetic field, and when the field lines converge, as they do towards the poles, particles whose velocity  $\mathbf{v}$  is not aligned with the field  $\mathbf{B}_0$  are repelled away from the high-field region and ultimately bounce back at a point that depends on the pitch-angle (angle between  $\mathbf{B}_0$  and  $\mathbf{v}$ ). If the pitch-angle is smaller than a certain value, the bounce point will occur below the altitude (around 110 km) at which the atmospheric density is high enough to collisionally slow down and untrap the particle from the magnetic field. Thus, the long-lived trapped particles all have velocities outside of this "loss cone" about  $\mathbf{B}_0$ . Artificial scattering of the particles has been proposed through interaction with VLF waves propagating along  $\mathbf{B}_0$ , whose rotating fields can be made to resonate with the gyro-motion of the energetic particles. Since the

waves themselves are to some extent trapped and will also bounce several times between the Earth's poles as shown in Figure 3, an opportunity exists for multiple interactions with a given particle. This translates into a smaller required interaction per pass, and the smaller required interaction per pass translates into radiating VLF waves reduced potentials (in this case the reduced potential is the amplitude of the voltage driving the antenna). The waves appropriate for electron scattering are in the VLF (10—100 kHz) whistler band; the pitch-angle scattering of high-energy electrons (< 2 MeV) by whistler waves has been widely studied<sup>1 2 4 16 17 19</sup>. The frequency of these VLF emissions is below the electron cyclotron frequency, but above the lower-hybrid frequency. Whistlers are right-hand elliptically polarized, with the same sense as the gyro-rotation of electrons around the Earth's magnetic lines.

From the theory of waves in a cold, collisionless, homogeneous plasma, the dispersion relation of the whistler mode propagating at an angle  $\theta$  with respect to the external magnetic field in an electron-plasma is given by

$$\mathbf{n} = \frac{\omega_{pe}}{\sqrt{\omega(\omega_{ce}\cos\theta - \omega)}} \quad (1)$$

where  $n$  is the index of refraction, which is the ratio of the speed of light to the phase velocity of the wave.  $\omega$  is the wave frequency,  $\omega_{pe} = \sqrt{q^2N/(m_e\epsilon_0)}$  and  $\omega_{ce} = qB_0/m_e$  are the electron plasma and cyclotron frequencies, respectively;  $N$  is the electron density,  $m_e$  is the electron mass,  $q$  is the elementary charge and  $B_0$  is the geomagnetic field. The plasma parameters depend on the L-shell and latitude, and the wave-normal angle  $\theta$  can be determined from ray tracing calculations. From this equation it can be seen that the minimum index of refraction corresponds to waves with  $\theta = 0$  degrees, and not too far from the lower-hybrid frequency this minimum is rather large (order of 10—20 degrees). It should be also noted that the magnetosphere is an anisotropic and inhomogeneous plasma, and the wave energy, in general, propagates in a different direction than the wave-normal vector. These rays, as opposed to individual waves, propagate in the direction of the group velocity. The group velocity is the direction in which waves exhibit positive interference; this group direction can be nearly perpendicular to individual waves for waves close to the resonance angle  $\theta = \theta_r = \cos^{-1}(\omega/\omega_{ce})$ . To accurately compute their trajectories the ray tracing equations have to be solved<sup>13</sup>. The ray tracing equations determine the variation of the ray position and wave-normal vector as a function of time for a given set of initial values of these quantities and a magnetospheric plasma model. Previous studies on ray tracing of whistler waves<sup>26</sup>

show that, under certain conditions, their group direction remains approximately aligned to the geomagnetic field and they bounce back when their frequency becomes comparable to the local lower-hybrid frequency. For this to occur, the refractive index surface must be finite at 90°. This is possible due to the contribution of ions to the dispersion relationship near the lower-hybrid frequency, which closes the refractive index surface around the perpendicular direction, and it allows whistler waves to perform several bounces along the magnetic field lines before they are lost due to dissipation. In addition, it has been shown<sup>27</sup> that these waves migrate radially and they settle on a particular L-shell in which the wave frequency is approximately equal to the equatorial lower-hybrid frequency.

The waves are supported, as described, by the cold background plasma. In turn, the fields associated with these waves exert forces on the small number of high energy electrons that populate the radiation belts. Electromagnetic waves resonate with the gyromotion of charged particles when the Doppler-shifted cyclotron resonance condition is satisfied

$$\omega - \mathbf{k} \cdot \mathbf{v} = \frac{m\omega_{ce}}{\gamma} \quad (2)$$

where  $\mathbf{k}$  is the wave-normal vector,  $\mathbf{v}$  is the electron velocity,  $m$  is an integer that determines the order of the resonance and  $\gamma = 1/\sqrt{1 - v^2/c^2}$  is the relativistic factor. For electrons resonating with whistlers where  $\omega < \omega_{ce}$ , we observe that the particles and the wave must travel in opposite directions. Given the wave frequency, L-shell and the loss-cone angle of the particles, Horne and Thorne<sup>15</sup> used this formulation to calculate the minimum equatorial parallel energy of electrons for cyclotron resonant interaction with various oblique electromagnetic waves at L=3 and above (over 20,000 km at the equator).

Whistler waves can be naturally occurring or artificially generated. Examples of naturally occurring waves are plasmaspheric hiss and lightning-induced whistlers. Lightning-induced whistlers are narrow band, audio-frequency electromagnetic radiation from lightning strokes that penetrate the lower ionosphere and travel through the magnetosphere along the magnetic field lines<sup>14</sup>. Plasmaspheric hiss are broadband incoherent emissions confined within the plasmasphere. Abel and Thorne<sup>1</sup> summarized the physical process involved in the electron scattering due to this kind of emissions. In addition, whistler waves can be generated from VLF ground-transmitter signals and space-borne antennas. Observations connecting VLF ground transmissions to electron precipitation have been studied in the past.<sup>18 28</sup> However, space-borne antennas are being proposed as a more power-efficient way of scattering the energetic

population of the belts; an example of that is the Demonstration and Science Experiments (DSX) from AFRL. The primary objective of DSX is to resolve critical feasibility issues of injecting VLF waves into the magnetosphere to determine how effectively this can be accomplished.<sup>12</sup> The goal is to assess the energetic electrons distribution and the perturbations and scattering effects on the particles due to these VLF waves. DSX is to be launched in the near future and its orbit will pass through the outer region of the inner radiation belt, the slot region, and the inner region of the outer belt. The DSX VLF transmitter is a center-fed dipole antenna of 80 meters in length (tip-to-tip), and the transmitter operates in two modes, high power at 3—50 kHz and up to 500 W (whistler waves), and low power mode (Boomerang waves) at 50—750 kHz at 1 W. The 80m DSX antenna length is not optimized for emission, but is a result of mechanical and expediency considerations. The usual selection criterion for vacuum antennas, in which a length of the order of half the wavelength minimizes the reactive power, is not appropriate for use on orbit in a plasma environment instead of vacuum. In fact, the wavelength itself ( $\lambda=2\pi/k$ , with  $k=n\omega/c$ ) is not a unique quantity as can be seen from the strong variations of  $n$  with direction (Eq 2).  $\lambda$  is maximum for  $\theta = 0$  degrees, and  $\lambda$  becomes zero at the resonance angle  $\theta_r$ .

The radiation resistance of an ionospheric electric dipole in the VLF regime can be approximated using the formulation developed by Balmain.<sup>6</sup> Using a quasi-electrostatic approximation, Balmain derived a formula, valid for any orientation of the antenna with respect to the geomagnetic field, for the complex impedance of a short cylindrical dipole in a magnetoplasma. This is permissible if the free-space wave-number  $k_0=\omega/c$  is small compared to the actual wavenumber  $k$ , or equivalently, if the index of refraction  $n$  is large. In magnetized plasmas, there are many regimes in which resonances occur, and then the index of refraction approaches infinity for some special directions; it is in the vicinity of these directions that most of the radiation power propagates. In the case of whistler waves, the resonance direction corresponds to wave vectors on a cone of included angle  $\theta_r = \cos^{-1}(\omega/\omega_{ce})$ , which is close to 90° about the geomagnetic field  $\mathbf{B}_0$ . Power then flows at an angle  $90^\circ-\theta_r$  on a cone close to  $\mathbf{B}_0$ . In addition, the sheath around a space-based LEO electric dipole is very thick, and so its capacitance is almost the vacuum capacitance, which is independent of the frequency and proportional to the transmitter length

$$C_{vac} = \frac{\pi L_a \epsilon_0}{\ln\left(\frac{L_a}{2r_a}\right)} \quad (3)$$

where  $L_a$  and  $r_a$  are the antenna length and radius, respectively. Short antennas would be ideal in terms of radiation resistance, because the relevant wavelengths (those near the resonance cone) are indeed very short; unfortunately, short antennas suffer the most from the small capacitance problem. In the whistler band, the capacitive reactance is tolerable for relatively short antenna lengths (several meters).

## CONCEPT OF OPERATIONS

### *Prelaunch and Launch*

TERSat is expected to launch on a standard ESPA ring. GSE design and launch vehicle interfacing are typical for ESPA payloads. TERSat will launch with partially charged batteries and will use an arming switch connected to the ESPA deployment signal to prevent other systems from enabling prior to deployment.

### *Commissioning*

Commissioning begins upon deployment from the ESPA ring. A signal will be sent from the ESPA ring to the power system to arm the system and allow the solar panels to begin collecting power to charge the batteries. The computer will also turn on at this time. As soon as the batteries are sufficiently charged, TERSat will begin to attempt communication with the ground. This may take several attempts if the spacecraft happens to be in a communications null at this point.

After communication is established, TERSat will check out the torque coils and detumble. TERSat will then proceed with turning on and checking out the rest of the satellite components one at a time after go-ahead commands from the ground after each step. Upon completion of checkout, the STACER antennas will deploy one at a time. Attitude sensors will verify the deployment and then reaction wheels will stabilize the spacecraft.

### *Normal Operations*

Normal operations will focus on performing the TERSat transmit/receive experiment. This experiment will be performed during sunlight at most every 5 orbits. During eclipse the satellite will turn off several components to save power, and heaters will be used to maintain temperature.

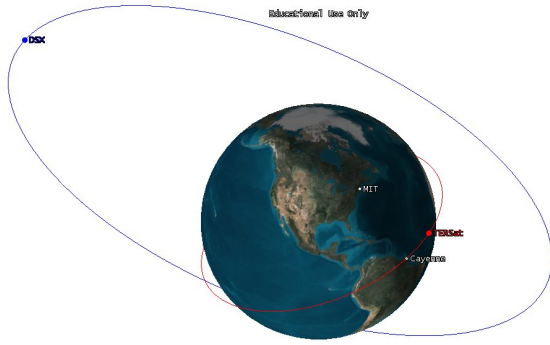


**Figure 4: TERSat Orbit Comparison with DSX**

Best-effort TERSat-DSX interaction experiments will focus on times when the two satellites intersect the same magnetic field lines and on times when the two satellites are physically closest. A comparison of the two orbits is shown in Figure 4 using a representative estimate of the DSX orbit that would need to be further refined and updated for actual experiment planning. DSX will be in a highly-elliptical MEO (6000 – 12000 km) orbit while TERSat will be in a circular LEO (550 km) orbit.

**End of Life**

Upon completion of its mission, TERSat will deorbit passively within 14 years.

**TERSAT DESIGN**

TERSat is a 16’’x16’’x12’’ (40.64 x 40.64 x 30.48 cm) and < 50 kg satellite. The TERSat payload will deploy two 2.5 m STACER antennas, transmit VLF waves using a student-designed and fabricated transmitter, and measure the strengths of the echoes and other VLF signals with a Stanford VLF receiver identical to the DSX receiver. The battery system consists of Ni-Cd batteries to power both the payload and the bus. The solar panels consist of a combination of UTJ Germanium cells and mono-crystalline Silicon cells and are body-mounted on 5 of the six outer structural panels. All electrical components are contained within the aluminum 6061-T6 chassis, including the batteries, computer, communications, and power electronics. The Attitude Determination and Control System (ADCS) uses three reaction wheels in conjunction with three customized torque coils. The spacecraft walls consist of skinned isogrid Al6061-T6 panels. Placement of these components is shown in Figure 5.

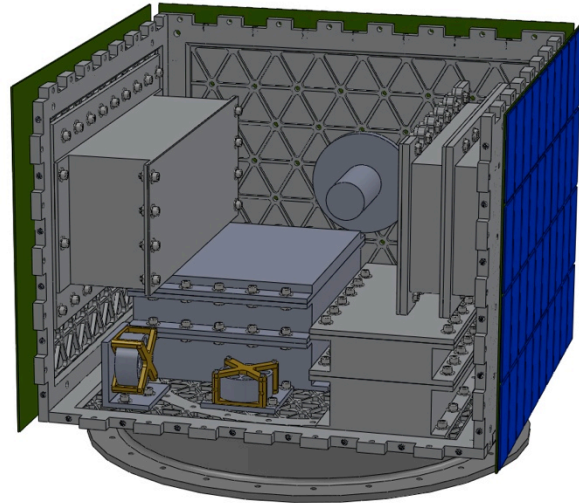


**Figure 5: TERSat Internal Components**

TERSat bus electronics take advantage of CubeSat technology, including a Pumpkin Motherboard and processor, a Clyde Space EPS, and an Espace S-band communication system. This enables standardization of interfaces and reduced wiring needs for rapid design and integration. It also reduces the qualification testing associated with custom parts.

**Technical Performance Measures**

The TERSat Program has tracked mass, power, data, and communications budgets to ensure design success. A master equipment list (MEL) has also been used to keep track of all system components. To validate these budgets, the QuickSat software tool has been used as a backup check. A summary of these budgets is in the following tables.

**Table 2: TERSat Mass Budget**

Subsystem	Subtotal (kg)	Margin	Mass Budgeted (kg)
Structures/Thermal	16.19	15%	18.62
Avionics Assy	2.04	15%	2.33
ADCS	0.84	15%	0.96
Power	7.00	15%	8.05
Wiring	4.00	15%	4.60
Payload	6.24	15%	7.27
<b>System Subtotal</b>	<b>36.3</b>	<b>System Total</b>	<b>41.7</b>

As shown in the mass budget in Table 2, the structures subsystem dominates the mass of TERSat. There are several reasons for this. To ensure structural stability under earlier high uncertainty of other subsystems, the structure was over designed. The panels are formed of isogrid aluminum rather than a more weight-efficient

and common composite-honeycomb sandwich design to reduce complexity for a student satellite. Also note that the satellite hardware is included as part of the structures subsystem rather than distributed amongst the other subsystems.

**Table 3: TERSat Power Budget**

Subsystem	Commis.	Nominal	Payload Tx	Safe Mode
Comm	4.6W	0.9W	0.3W	4.6W
Avionics	2.5W	2.5W	2.5W	2.5W
ADCS	2.8W	3.5W	4.0W	0.4W
Thermal	7.5W	7.5W	0.0W	7.5W
Payload	0.2W	0.0W	40.0W	0.0W
Power	2.1W	1.7W	1.5W	0.9W
<b>Total</b>	<b>19.9W</b>	<b>16.2W</b>	<b>48.2W</b>	<b>16.0W</b>

The TERSat power budget is shown in Table 3. In most modes, the thermal subsystem dominates TERSat power usage. This is because the thermal system powers heaters for temperature-sensitive components such as batteries when the rest of TERSat does not produce enough power to compensate in heat production.

One interesting feature of the power budget is the payload power during operation. While transmitter

power can be estimated based on the plasma interaction models, only the input voltage (100-600V) can be known with certainty as the radiated power depends on how well the transmitter circuit is tuned to the plasma environment, which cannot be known or adjusted until experiments commence on-orbit. Measurement and characterization of the power drawn is one of the expected results of the experiment.

***Payload***

The TERSat payload consists of three key elements: the STACER antennas, the VLF transmitter electronics, and the Stanford Wave-induced Precipitation of Electron Radiation (WIPER) VLF receiver. The transmitter electronics and the receiver each have a dedicated chassis, and although electrically connected, the STACER antennas mount to opposite panels to create a dipole when deployed.

To determine the optimal design of the payload transmitter electronics, a Matlab simulation of electromagnetic radiation in a plasma<sup>25</sup> predicted the expected power output for a range of inductance values assuming a 600 V input. The results of this analysis are shown in Figure 6. As the inductance values were tuned from 0.3 H up to 1 H, the power output and resonant frequency of the circuit varied.

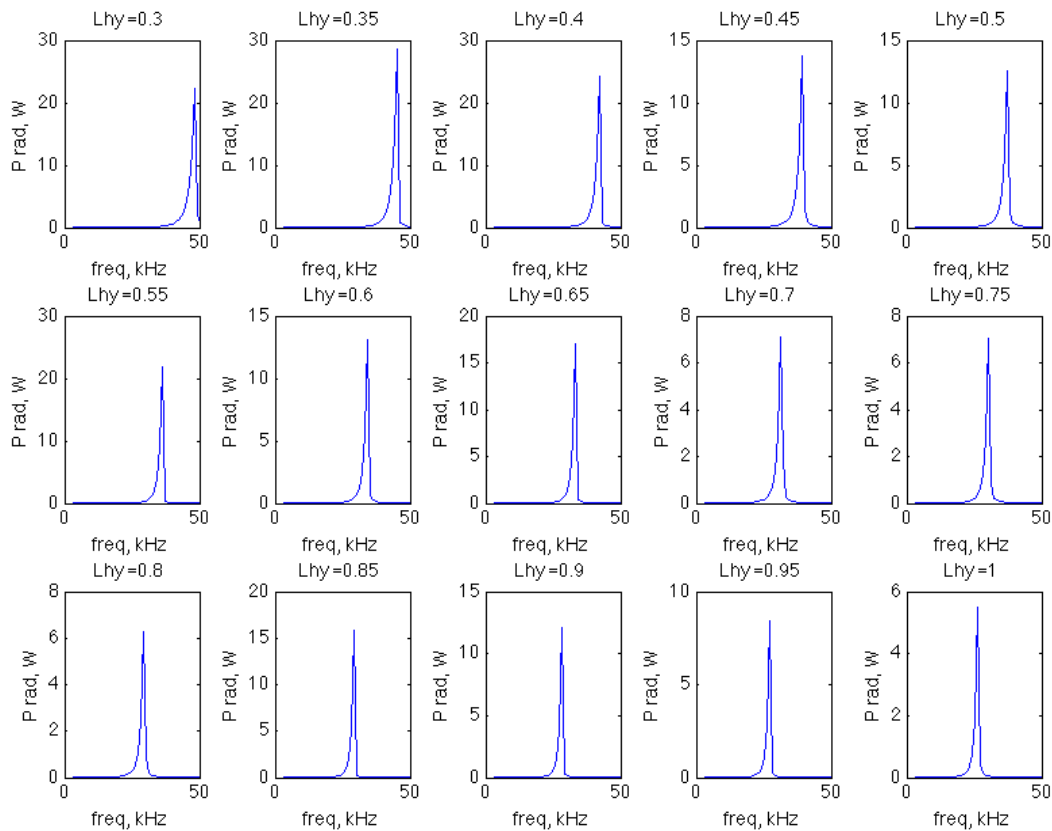


**Figure 6: Simulation of TERSat Transmissions at Varying Inductance Values**

The final design parameters are shown in Table 4. The antenna length of 5 m was found to be sufficient for experimental needs while still short enough to be easily accommodated by existing facilities when deployed for testing. A peak voltage of 600 V is expected to provide sufficient margin on the minimum voltage of arcing in a plasma.<sup>23</sup>

**Table 4: Key Payload Design Parameters**

Subsystem	Subtotal (kg)
Antenna Length	5 m
Peak Voltage in	600 V
Frequency Range	3—50 kHz
Inductance Range	0.2—3.0 Henry

For the antenna, the STACER system developed by Ametek Hunter Spring was selected. The STACER is a coiled spring-type mechanism, which can extend to

significant lengths in the axial direction<sup>5</sup>. For lengths less than 10 m (35 ft) the STACER can be purchased as a pop-up one-time deployment model using stored elastic energy to fully deploy. Options for the STACER include a wide choice of materials and coatings that should meet the science needs of TERSat, including electrically conductive variants.

The key benefits of the STACER system are its versatility and flight heritage. Because each STACER is custom designed for its mission, it is possible to purchase a pair of devices that meet all of TERSat’s mission requirements. TERSat will use a conductive Beryllium-Copper alloy. This material was selected as it provides both structural rigidity as well as the electrical conductance needed for the science mission. Finally, the STACER system has flown on approximately 600 missions as an actuator for, or a key component of, deployable booms and antennas.

TERSat has purchased a STACER and housing for testing. Designs for how the STACER will integrate

into the bus and payload has begun, and deployment tests and characteristics are being currently underway. At the completion of testing, this information will be used to further refine the control algorithms used by ADCS to maintain stability. Concurrent with the deployment characterization, a new deployment mechanism is being developed to improve the reliability of STACER deployment using a frangibolt-based system. This new deployment system would replace the standard pullpin system, and has heritage on similar deployable-equipped missions.

The TERSat transmitter will radiate VLF waves for 1 to 30 seconds within the range of 3—50 kHz. At least 600 V will be supplied from the transmitter to the antenna in order to radiate these waves. The Ni-Cd batteries will initially supply 24 V to bias the H-bridge and 12 V to bias the inverter and H-bridge control chip. An additional low-voltage logic signal will be the input to the H-bridge control chip in the form of a square wave, using a microcontroller pulse to set the wave frequency. The H-bridge will trigger off of the microcontroller pulse and continuously switch the direction of the current supplied by the Ni-Cd batteries and form a full square wave. The output voltage will then be fed into a transformer that will be used to step up the output voltage to the desired maximum of 600 V. This stepped-up voltage will be supplied to the payload in the form of a sinusoidal waveform (using an RLC circuit to tune/impedance match, which will also filter out high-frequency components of the square wave) and will be used to radiate VLF waves. The transmitter voltage and current will be measured and their phase tracked in order to provide power estimates as well as information on the impedance match. It is important to characterize the impedance of all components in the transmitter as a function of frequency during testing.

We have built an engineering model of the transmitter system and have performed both low and high voltage and frequency tests and demonstrated the ability to generate a sinusoidal waveform as well as characterize its voltage, current, and phase behavior to power the VLF transmitter. Instead of Ni-Cd batteries, for the engineering model, a voltage supply is being used to supply 12 V to the H-bridge instead of using the Ni-Cd batteries. As a substitute for the microcontroller, a function generator is currently being used to generate the low-voltage pulse at the desired operating frequencies (the resonant frequency of the engineering model is approximately 17 kHz). A transformer is being used to step up the H-bridge output voltage from 6 V to up to 1200 V (600 V center tap). Test points in the circuit include the input voltage signal to the H-bridge, the output voltage across the H-bridge, and the output voltage across the transformer. Preliminary tests have

shown that at a low voltage and frequency, the H-bridge and transformer will be able to generate high-voltage VLF sinusoidal output.

Further testing will be performed to use the Ni-Cd batteries with the H-bridge engineering model instead of using a power supply to provide voltage. A PIC33 or PIC24 microcontroller will next be included in the testing procedure to eliminate the use of the function generator. However, the current H bridge that is being used in the engineering model will inform the final flight design, and so further tests on the engineering model across the full 3—50 kHz range are needed.

The TERSat VLF receiver uses the Stanford WIPER VLF receiver chip. This chip has a wide bandwidth and is capable of receiving from 100 Hz to 1 MHz<sup>22</sup>. It is also low power, requiring less than 0.5 W to operate. This chip will be placed on a PCB with supporting electronics. EMI filtering will maintain the sensitivity of the chip and scrub the incoming signal from the dipole antenna. The receiver chip will interpret the signal and the primary avionics computer will process the data. The WIPER chip and supporting electronics will be housed in an aluminum chassis mounted to a side panel of the spacecraft.

To familiarize the team with VLF receivers and to enable FlatSat testing prior to transfer and incorporation of the WIPER chips, two Interactive NASA Space Physics Ionosphere Radio Experiments (INSPIRE) VLF Receiver Kits were assembled. Audio output was tested according to INSPIRE instructions and data output was confirmed using an oscilloscope and microphone. After the preliminary familiarization with the INSPIRE kits, an Ettus Universal Software Radio Peripheral (USRP) was purchased along with both VLF transmit and receive daughterboards as well as S-band daughterboards and integrated with GnuRadio, a software defined radio (SDR) package. The Ettus VLF receiver setup has been successfully used to detect transmission from the VLF transmitter engineering model as well as detect other VLF sources nearby.

### **Power**

The Power Management and Distribution system begins with the solar panels, which supply the primary power for the system. Five body-mounted solar panels sit on the  $\pm x$ ,  $\pm y$ , and  $+z$  faces of TERSat as shown in Figure 7. The panels are made up of a mixture of Monocrystalline Silicon and Ultra Triple Junction Germanium cells. These have efficiencies of 16% and 28.3% respectively.

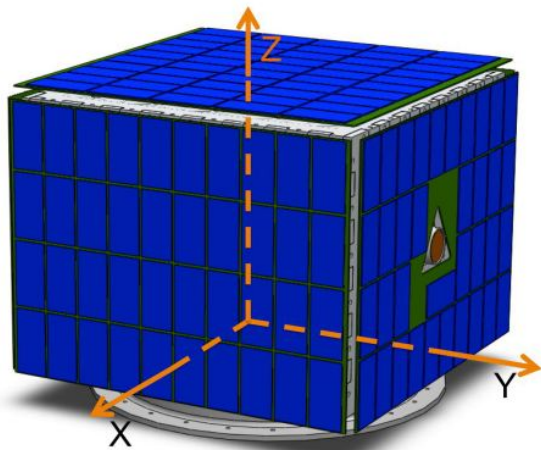


**Figure 7: Body Mounted Solar Panels with Axes**

The power from each of the solar panels is regulated by the Maximum Peak Power Tracker (MPPT) and then delivered and monitored by the Battery Charge Regulator (BCR) which is connected to two Nickel Cadmium (NiCd) battery packs. One battery pack is dedicated to powering the system bus and delivers 12 V to the Power Distribution Unit (PDU). From here, power is delivered on three rails to the avionics subsystem at 3.3 V, 5 V and 12 V. The avionics subsystem distributes power to each subsystem as needed. See Figure 8 for the power system block diagram. The second battery pack is devoted to the transmitter and antenna drive system. This delivers power to the H-bridge and payload transmitter electronics.

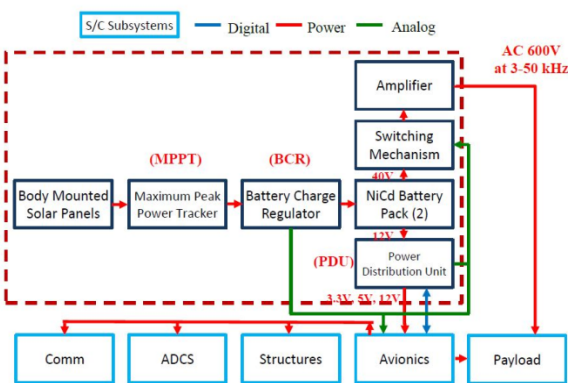


**Figure 8: Power Block Diagram**

### Structures and Thermal

The structure of TERSat is based around a skinned isogrid bus 12” high and 16” on a side, fitting well within the UNP volume requirements. The isogrid

panels incorporate an interlocking edge feature allowing for simplified assembly without the need for internal bracketing at the panel junctions. Within the spacecraft bus, key electronics are housed within four subsystem component boxes mounted directly to the isogrid structure. The two deployable STACER antennas are mounted within the bus along the spacecraft’s Y-axis to support TERSat’s main science mission.

The skinned isogrid structures used on five of the six sides allows for major mass savings while maintaining a stiff structure with isotropic properties. The holes at the isogrid nodes also allow for multiple internal and external attachment points for subcomponent boxes, the body mounted solar arrays, and any other components. The structure’s skin also provides additional radiation shielding for internal components. The isogrid design was completed using NASA’s Isogrid Design Handbook<sup>19</sup> resulting in a structure optimized to meet the 100 Hz minimum first fundamental frequency requirement set by UNP.

The subcomponent boxes housed within TERSat are treated as individual assemblies prior to system integration. This design allows for bench testing to be completed in a FlatSat configuration, which simplifies testing procedures. When testing is completed, each of the six bus panels will be assembled separately before being assembled together into the final flight configuration. For final testing, the bus will be assembled with temporary hinges, allowing the structure to be “unfolded.” This will again simplify the hardware checkout procedure. When final checks are completed, the hinges are removed and the interlocking edges of the isogrid planes are mated and bolted together.

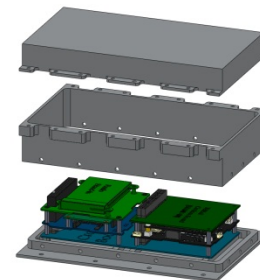


**Figure 9: TERSat Avionics Box Components**

Each of the component boxes have been designed around the components they house. Internal components, or expected volume envelopes, were modeled with SolidWorks, and the boxes were built around them. This process ensured that appropriate space was included for the components and wiring,

while also ensuring proper attachment points were modeled. For manufacturability, each box except the battery box has a layered design. At the bottom of each box there is a mounting plate, which facilitates attachment to the isogrid structure, and serves as a mounting plane for internal components. Attached to the bottom plate is a box section open at both faces, allowing for simple fabrication utilizing a waterjet and post machining with a standard mill. This bottom box section bolts to a mounting lip on the bottom plate with 90° edges, minimizing EMI interference. At the top face of this bottom box section, bolt holes are placed to allow for attachment of further layers or the box top section. The bolt attachment flanges are designed to capture the bolt without the need for nuts, simplifying the assembly process. Furthermore, they are designed to allow for easy access to the mounting bolt pattern on the base plate. The final section of the box is a top, which mounts directly to the middle box section using bolts along the perimeter. Due to the size of the battery box, the sectioned box design previously discussed is not a feasible option. Therefore, additional modeling is underway for this subcomponent box.

#### Structural Analysis

Finite element analysis considered the +/- 20 g static load conditions per the UNP guidelines. However, the model was set up such that random vibration inputs could be analyzed in preparation for future testing and model validation. The stress margins were computed for a +/- 20 g load input in each axis with a Factor of Safety in Yield Stress ( $FS_y$ ) of 2 and a Factor of Safety in Ultimate Stress ( $FS_u$ ) of 2.6 per the UNP Stress Analysis guidelines. This analysis was built in MSC/Patran and run using Nastran.

The TERSat modeling approach consists of a detailed finite element analysis (FEA) model with all structural elements and hand calculations for fastener and pressure analyses. Modeling began with hand calculations using plate theory and the NASA Isogrid Handbook, and then progressed through increasingly detailed models to the current version.

The TERSat finite element model is shown in Figure 10. The second image has two side panels and the end panel removed for clarity. The bus is modeled using a combination of shell elements for the isogrid skin and beam elements for the isogrid ribs. The isogrid nodes are equivalenced so that the beam elements and shell elements transfer forces properly to each other. The rim of the isogrid was modeled by quadrilateral (quad) shell elements, with equivalence nodes to mate with the isogrid boundaries.

Component boxes are modeled as tetrahedral (tet) elements. The density of these component boxes was adjusted to account for the masses of the component contents, such as parts, connectors, and wiring. To estimate this density, the conservative “density of water” rule of thumb was applied, multiplying the volumes of each box by the density of water. The density of each box was then adjusted to meet this mass. The masses were checked against the mass budget prediction to ensure each exceeded the items called out in the budget. The Lightband adapter ring was also modeled as tetrahedral elements.

Connections between components were made using RBE2 elements. This connection type did not allow for good bolt force calculations in the finite element model (FEM), but the future work section will address this point. Fastener analysis information came from using extremely conservative loading information and using hand calculations to estimate bolt stress. The RBE2 elements used the nodes around the top of each through hole as dependent nodes and a node on the mounting surface as the independent node. For all connections except the lightband mounting connection, only the nodes on the edge of the through hole were used, and not the nodes a full bolt head radius out, leading to nonphysical concentrated forces around mounting locations.

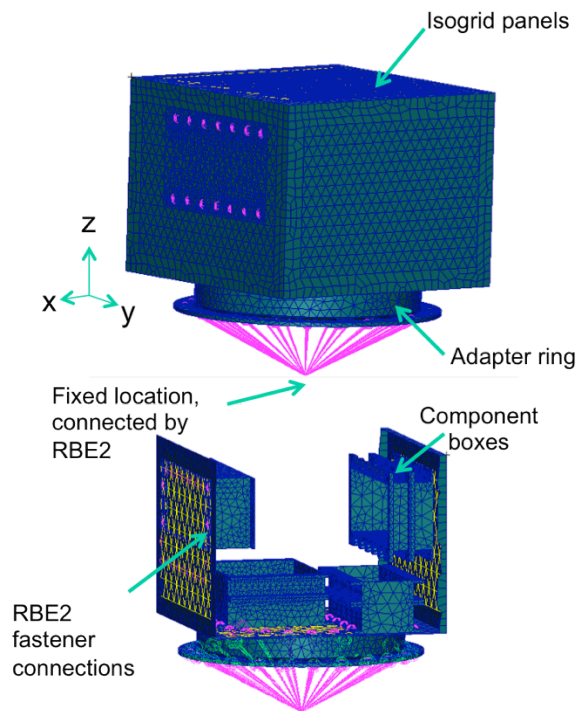
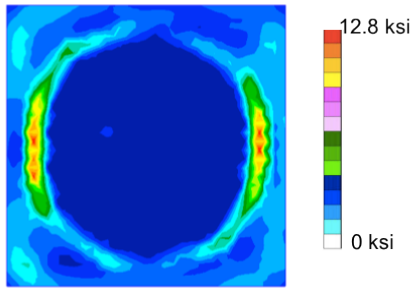


Figure 10: TERSat Structural Model

The conservative analysis indicates positive margins of safety (MOS) on all components for the UNP input loading guidelines and that the design meets the 100 Hz requirement. The minimum MOS is 0.21, indicating the structural design is sound. This MOS occurs on the battery box for ultimate stress. The next lowest MOS is on the ESPA interface panel, with a  $MOS_u = 0.26$ . The stress locations were along the ESPA mounting interface bolt ring, as shown in Figure 11.



**Figure 11: TERSat FEA -Z Plate Stress**

Initial modal results with an isogrid for the lightband interface panel resulted in a natural frequency of 101 Hz. However, given a large expected margin in the mass budget, this plate was switched to a flat plate, allowing for greater margin in the frequency and greater flexibility in the component box mounting design if prototyping indicates a need for redesign.

**Table 5: TERSat Modal Analysis Results**

Mode number	Frequency [Hz]	Description
1	116	Full S/C rocking
2	126	Full S/C rocking
3	166	Side panel drum mode with rocking motion
4	194	Top panel drum mode
5	222	Avionics box panel mode

### Thermal Analysis

Design of TERSat's thermal control system is driven by a challenge common to many small satellites: a small external surface area. Having a small external surface area limits not only the power available to heaters due to restricted area for solar panels, but also limits exposed area that can either absorb energy to heat the spacecraft or radiate heat to cool it. These limitations do not allow for large margins in thermal design and therefore require thorough thermal modeling and testing.

COMSOL was used as the primary modeling method

because it can provide information about specific component boxes more easily than hand calculations. Figure 12 shows the thermal model used in COMSOL which includes the spacecraft bus, the four internal component boxes, and the battery bank. The antenna and individual components besides the batteries are not yet included. Most of the model is constituted of aluminum, but all bus faces are then covered in Multi-Layered Insulation (MLI). Additionally, all bus faces except the  $-z$  face are shaded by offset solar panels. Each box is equipped with a heater capable of outputting 10 W.

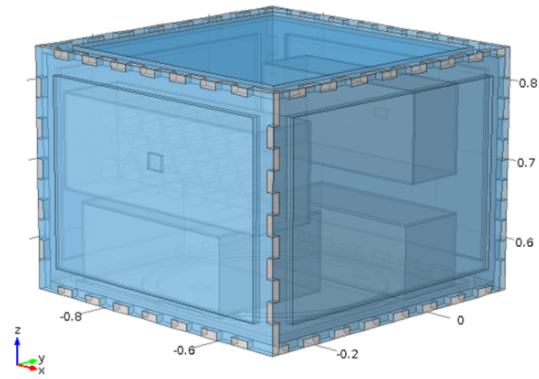


**Figure 12: TERSat Thermal Model**

Initial analysis indicated that many components reached temperatures significantly lower than their survival limits. This led to the addition of heaters in key component boxes. Figure 13 shows the thermal cycle TERSat is predicted to experience during nominal operations with a 10 W heater operating at an 84% duty cycle. All components are within their acceptable temperature ranges.

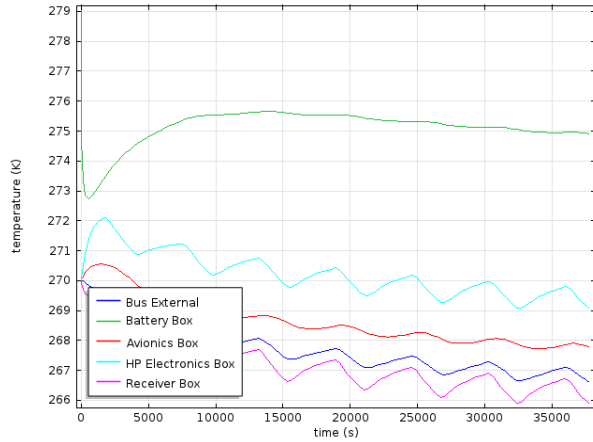


**Figure 13: TERSat Thermal FEA Results, Normal Mode with 10W Heaters**

In summary, due to the offset solar panels shading most TERSat’s faces, the satellite receives less heat from its external environment than is adequate to heat the satellite to acceptable temperature ranges without additional heat. For this reason, TERSat must rely on internal heat production and thermal insulation to maintain the necessary temperatures. On the other end of the spectrum, TERSat never approaches the hot end of its temperature limitations so cooling methods are not required. Finally, all analysis predictions must be verified by testing.

### ADCS

The TERSat ADCS design is straightforward; the concept of operations does not require any unusual pointing modes. One design difficulty results from the deployed STACER antennas, which may impart some flexible body dynamics. However, the pointing requirements derived from the science mission do not require particularly precise pointing (15° threshold).

The ADCS provides attitude and position knowledge using a combination of fine sun sensors, a magnetometer, and an inertial measurement unit (IMU). Attitude control is maintained through the use of three orthogonally-arranged reaction wheels, periodically desaturated by three likewise orthogonally-mounted magnetic torque coils. For the purposes of structural design simplicity, the dimensions of the torque coils have been specified to match the sizes of the inside of the bus panels, with dimensions of 38.5 cm by 38.5 cm (area 1482.25 cm<sup>2</sup>) and 38.5 cm by 28.5 cm.

The external torque due to environmental factors experienced by TERSat during its mission is expected to be very small, with an order of magnitude such that

the external torques could be countered entirely through the use of torque coils. However, reaction wheels will be the primary actuators to address the desire to promptly realign the spacecraft with respect to the magnetic field during observations, to minimize the effect of electromagnetic interference from torque coils during VLF transmit/receive operations, and to broaden orbital inclination options by reducing the dependence of ADCS on the gradient of the magnetic field.

Factors affecting the selection of reaction wheels and of magnetic torque coil parameters (current, number of turns) include the saturation and desaturation time, thermal and response properties of the coils, and cost.

The reaction wheel controller is a simple proportional controller acting on the error between the estimated pointing and the commanded pointing. This simple controller works because of the mostly linear dynamics involved with nadir-pointing satellites. The torque coils currently operate with a B-dot magnetic control law. The B-dot control law is designed for rate damping, making it well suited for use during detumbling. The B-dot control law is as follows:

$$\boldsymbol{\tau} = \mathbf{m} \times \mathbf{B} \quad (4)$$

where  $\boldsymbol{\tau}$  represents the control torque vector,  $\mathbf{m}$  represents the magnetic dipole moment of the torque coils, and  $\mathbf{B}$  represents the local magnetic field of the Earth.

To test these control laws and actuator selection, a model of the TERSat ADCS was built in MATLAB Simulink, as summarized in Figure 14. This model consists of four major parts: a module that determines the external environmental forces and torques acting on the satellite (including drag, gravity gradient, magnetic disturbances, solar pressure, and the magnetic torquers), a module that describes the spacecraft’s rotational dynamics and the dynamics of its actuators, a module that determines the rotation matrices and transformations between the various required reference systems, and a module containing the controller logic.

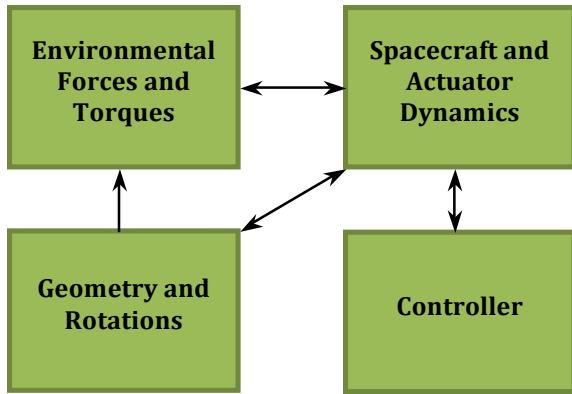


**Figure 14: ADCS Simulink Model Outline**

Modelling has not yet been completed on sensor dynamics or an estimator (the controller thus uses full-state feedback).

In order to evaluate the effectiveness of the reaction wheel varieties being considered (10, 30, and 60  $\text{mN}\cdot\text{m}\cdot\text{s}$ ), the simulation was run for several orbits to examine desaturation duty cycle. These trials used the deployed-antenna configuration, which would be subject to larger torques and so represents the more difficult control case. The 10-  $\text{mN}\cdot\text{m}\cdot\text{s}$  wheels did not demonstrate sufficient capacity, requiring too great a fraction of time on magnetic momentum desaturation (and thus too little time available for science data collection). Rerunning the simulation with the 30- $\text{mN}\cdot\text{m}\cdot\text{s}$  wheels while desaturating at only half the momentum storage capacity of the wheels, on the other hand, showed very good behavior, depicted in Figure 15 and Figure 16.

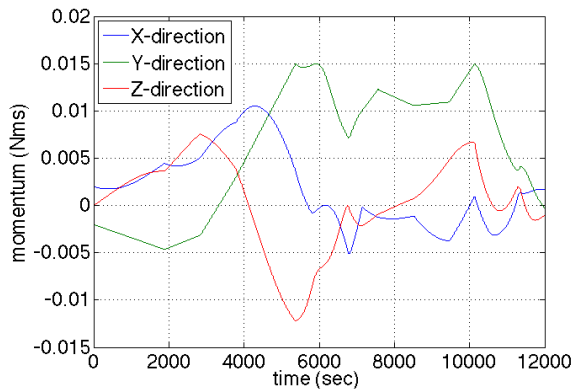


**Figure 15: Reaction Wheel Momentum Storage for Two Orbits**

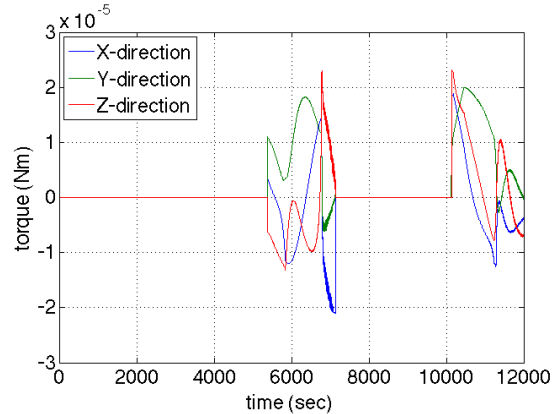


**Figure 16: Commanded Magnetorquer Torque for Two Orbits**

Figure 15, with the reaction wheel momentum in each axis as a function of time, shows that the system properly identifies when one of the wheels has reached its threshold value, 15  $\text{mN}\cdot\text{m}\cdot\text{s}$  (in this case half of its actual saturation limit of 30  $\text{mN}\cdot\text{m}\cdot\text{s}$ ) and then drives all three wheels close to zero within approximately half an orbit. Figure 16 showing the torque coil activity, depicts their activation upon the reaction wheels reaching the momentum threshold and then deactivation when the wheel momentum falls to within a small tolerance of zero.

With the baseline torque coil design, the 30-  $\text{mN}\cdot\text{m}\cdot\text{s}$  reaction wheels will be sufficient to give the required attitude control while also leaving large windows of time during which useful payload data can be collected.

### *Avionics and Communications*

TERSat's avionics system has two main components, the Onboard Avionics Computer (OAC) and the Ground Station. The OAC handles all general flight operations, including sensor reading, attitude estimation and control, and communications with the Ground Station. The Ground Station, located at the MIT Control Center, relays commands to the Open System of Agile Ground Stations (OSAGS) to control TERSat from the Earth. The avionics system relies on a threaded real-time operating system to manage the required periodic and concurrent control, computation, and transmission tasks.

The OAC hardware is designed around COTS boards. These include a pluggable processor module with a Microchip dsPIC24F and a motherboard manufactured by Pumpkin Inc. The micro-controller interfaces with other subsystems via UART, SPI, I2C, PWM, and ADC buses, and communicates with the ground through one transceivers and two patch antennas. The boards were chosen for being a low-cost, high reliability COTS

option for spaceflight. The micro-controller has 256 KB of program memory and 16 KB of RAM,<sup>10</sup> enough to satisfy mission requirements with extremely conservative margins.

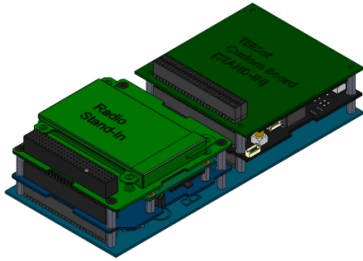


**Figure 17: Onboard Avionics Computer, Payload Telemetry System, Clyde Space EPS, and Custom Interface Board**

Analysis suggests that the NAND memory on the Cubesatkit PPM (64Mb Flash) and Motherboard (8Gb SD Card) has sufficient storage to satisfy all TERSat data storage requirements. Preliminary analysis of CPU, Memory, and Bus utilization estimates suggest that the amounts of PIC memory, Bus utilization, and CPU processing are below the maximum limits even in the worst-case scenario. More analysis of the PIC processing throughput still needs to be completed to determine if the dsPIC24F has sufficient processing capability. If margins of error are less than the ideal system requirements, then the data storage strain can be reduced by reallocating tasks or by lowering the frequency at which some tasks are performed. The data storage computing budget for the OAC is outlined in Table 6. For certain operation modes the expected percentages of storage used exceeds 100% of the flash total memory available after a write period approximately 480 minutes. TERSat will maintain its data logging capabilities by writing excess memory to the onboard SD memory card.

**Table 6: TERSat Data Storage Budget**

Mode	Flash		SD	
	Mode Duration (min)	Storage Used (%)	Mode Duration (days)	Storage Used (%)
Safe/Start Up	90	11%	3	1%
	480	21%	7	2%
Detumble/Stabilize	90	33%	3	2%
	480	175%	7	4%
STACER Antenna Deployment	90	1%	3	0%
	480	3%	7	0%
System Check	90	21%	3	1%
	480	113%	7	2%
Nominal Operations	90	35%	3	2%
	480	187%	7	4%
Mission Operations	90	45%	3	2%
	480	240%	7	5%

The software run by the dsPIC24F is based on the ThreadX Real Time Operating System by Express Logic, an open source C based software kernel. TERSat's software is coded in C and designed to take advantage of ThreadX's capabilities to run threads and ensure that specific threads meet required deadlines. The control logic for this is provided by the Application Layer in the TERSat software architecture, which handles all flight software functions in each of the satellite operational modes as well as transfer between those modes. Mission operations are managed by the High Level Task Manager, based on the JPL Mission Data System (MDS) model.<sup>7</sup> The High Level Task Manager uses knowledge of the current state to designate control to the low-level task manager and ADCS system, which carry out the assigned action or sensing requirement. The system is designed to check that commands produce their desired results, allowing the High Level Task Manager to have closed-loop control of the system.

The low-level task manager handles execution of commands to individual subsystems, including thermal and power sensing as well as science data collection and actuator control. At this level, all subsystem command state machines are at the same hierarchy level but not the same priority level, so although separate commands for distinct subsystems cannot be executed simultaneously, higher priority threads can be called during another thread's operation through the use of software interrupts. Task priority levels are hardcoded into the software via the ThreadX Operating System.

Testing the TERSat software has been the focus of the TERSat FlatSat development phase, which demonstrates the integration of hardware and software with other subsystems. For FlatSat development, power resistors and software simulators serve as stand-ins for some components to allow testing of software operations for components that have not yet been acquired. Tests were considered successful if telemetry and/or commands could be exchanged between the user and the hardware during run-time; success was achieved in the implementation of GPIO, PWM, UART, and ADC buses.

In addition to demonstrating avionics interfaces with other subsystems, work has been done to calibrate the magnetometer and IMU on the OAC. Tests of the IMU gyros were performed on a rotating table to determine the necessary count offset. The magnetometer was calibrated by subjecting it to uniform magnetic fields of varying strengths in the center of a pair of Helmholtz coils. Future work will include calibration and testing

of TERSat’s other state sensors, including the sun sensors, thermal sensors, and power sensors.

The communications subsystem includes the hardware and software infrastructure necessary for the downlink of payload and telemetry data, and the uplink of spacecraft commands. An Espace, Inc. Payload Telemetry System’s S-Band Transceiver (PTS-SBT) designed for LEO applications drives the on-orbit uplink and downlink segment of the TERSat communications system. The transceiver interfaces with two customized patch antennas located on the opposite ends of the satellite. The spacecraft communicates with the ground on S-band frequencies via the OSAGS located in Kwajalein, Cayenne, and Singapore.

The OSAGS was selected due to its encryption capability, lower programmatic risk, and the ability for the TERSat Team to access the control center, which is on campus at MIT. Figure 18 presents the locations of these stations. Data is transferred between each ground station and MIT via a TCP/IP connection. Each of the ground stations is equipped with a 2.3 m diameter parabolic dish antenna. Estimated noise temperatures are documented in the TERSat Link Budget which is summarized in Table 7. Presented in the table are the best/worst-case downlink margins and uplink margins. The link margins are greater than 3 dB, which has been established as the minimum margin allowed between the required energy to noise ratio needed for a bit error rate of 1/100,000 and the predicted energy to noise ratio.

**Table 7: TERSat Link Budget**

	<b>Downlink Worst Case</b>	<b>Downlink Best Case</b>	<b>Uplink Worst Case</b>	<b>Uplink Best Case</b>
Equivalent Isotropic Radiated Power [dB]	1	1.5	38.57	39.07
Rx Antenna Gain [dB]	32.27	32.27	6	6
Free Space Loss [dB]	-163.42	-154.11	-162.70	-153.39
Total Pointing Loss [dB]	-2.17	-2.17	-2.17	-2.17
Ionospheric Loss [dB]	-1	-1	-1	-1
Atmospheric Loss [dB]	-0.3	-0.3	-0.3	-0.3
Loss due to Rain [dB]	-2	-2	-2	-2
Demodulator Loss [dB]	-1.5	-1.5	-1.5	-1.5
Implementation Loss [dB]	-1	-1	-1	-1
<b>Eb/No [dB]</b>	<b>14.01</b>	<b>23.83</b>	<b>24.25</b>	<b>34.07</b>
Data Rate [dBps]	50.61	50.61	50.61	50.61
Boltzman's Constant [dbW/H z*K]	-228.6	-228.6	-228.6	-228.6
System Noise Temperature [dBK]	25.85	25.85	27.63	27.63
<b>Db/No required [dB]</b>	<b>9.6</b>	<b>9.6</b>	<b>9.6</b>	<b>9.6</b>
<b>Margin [dB]</b>	<b>4.41</b>	<b>14.23</b>	<b>14.65</b>	<b>24.47</b>

The PTS-SBT has a form factor of approximately 3.55 in x 3.775 in x 17 mm and draws 4 Watts of power during transmission and 2.5 Watts during uplink. Given these power parameters, transceiver power can be drawn from a 7.5V supply. The PTS S-Band transceiver receives at an S-Band frequency range of 2.025–2.120 GHz and transmits at an S-Band frequency range of 2.200–2.300 GHz. The downlink data rate can vary from 63 kbps to 2138 kbps with QPSK or OQPSK modulation, depending on the elevation angle. The CPFSK modulated uplink has a data rate of 348 – 7182 kbps, again depending on the elevation angle.

Antenna parameters such as the internal impedance, central frequency, and bandwidth of downlink and uplink have been chosen in order to meet mission and system requirements. One antenna is placed on the side of the spacecraft normally facing the earth. The other antenna is placed on the side of the spacecraft adjacent

to the side facing the earth. This placement will provide coverage in the event of a primary antenna failure during normal operation, and it will also provide more hemispherical coverage during initial tumbling.

Along with the OAC, the PTS transceiver is housed inside of a securely mounted, radiation/EMI shielded aluminum box (Avionics Box). The PTS-SBT will communicate with the Onboard Avionics Computer over a SPI and UART connection. A male SMA Cable rated for space environments will connect the transceiver to the each of the two S-Band patch antennas via a 3 dB splitter. The PCBs containing the patch antenna will be mounted to the outside of the  $\pm Y$  structural isogrid panels.

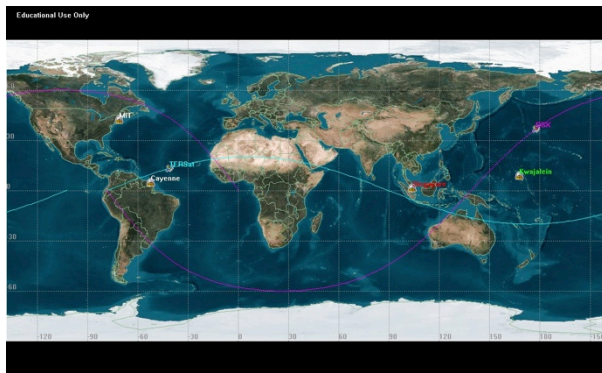


**Figure 18: OSAGS Ground Stations Relative to TERSat Orbit**

Communication with the ground stations will be performed at least three times a day with a high probability of link access every two 90 minute orbits. The placements of ground stations relative to the TERSat nominal orbit are shown in Figure 18. Due to the expected link session periods of approximately 541 seconds a downlink rate of 115,000 bit/sec was chosen to ensure complete discharge of telemetry data on a daily basis. The maximum data accumulation rate is 4,400 bit/sec; however, this rate can be altered in real-time to ensure that the maximum data accumulation total remains less than the maximum data storage capacity.

Each link session is initiated by the ground station. Once the satellite catches a setup message transmitted from the ground station and verifies that it has been correctly received, the satellite transmits an acknowledgement packet. The link session is then open and the ground station sends command packets and waits for acknowledgement. The satellite then downlinks telemetry data followed by any science data.

The ground station finally sends a message closing the session.

TERSat communications software receives uplink packets, identifies the packet type (via unique 12-byte headers), verifies that the packet has not been corrupted (via 8-bit Cyclic Redundancy Check and Automatic Repeat Request protocol methods), and passes command data to the avionics board microprocessors. TERSat communications protocol follows the Open Systems Interconnection model for communications systems in which the physical and data link layers of the TERSat communications protocol are implemented directly by the PTS. The transport layer handles packet definition, and ensures that each transmitted packet is received completely and correctly.

### **PATH FORWARD**

Moving forward, TERSat will transition from a heavily focused design phase to a build phase. Preliminary steps for this phase have already occurred through the development of FlatSat demonstrations; however, these FlatSat demonstrations only test the functionality of individual subsystems. Upon documenting FlatSat testing results, the build phase will begin. The build phase, which occurs at the beginning of May, will encompass the building of the engineering test unit (ETU) for the Proto-qualification Review (PQR) in August. The ETU will be a fully functional model of the final flight unit. The beginning of the build phase will involve ordering and locating all parts to be used in the ETU. Upon receiving the isogrid panels, a fit check will be performed to ensure that the panel connections are accurate.

Once the component boxes are received, installation of components within the boxes will begin. This process will make up a bulk of the ETU integration process. Component box building will involve installation of components, application of adhesives, and wiring. Next, all component boxes will be installed into the frame of the satellite and a second fit check will be performed.

During the process of ETU assembly, both individual and integrated functionality tests will be performed on the components to assess operation and durability of the satellite. Individual testing will evaluate the operation of individual components. Integrated testing will analyze the interactions between subsystems by testing communication among components, verifying correct power levels are being supplied to the subsystems and payload. ETU testing will occur over a three-week period and will continue beyond PQR.

After PQR, the functionality of the satellite will continue to be improved and expanded by incorporating

feedback from the review in anticipation for the Flight Competition Review (FCR). Select components will be replaced with space-qualified versions and more rigorous testing will be performed to test the functionality of the satellite.

## SUMMARY

The TERSat student satellite project permits students to gain experience in all aspects of small satellite design and implementation. The program has passed CDR and integrated FlatSat testing is underway. The design includes key technologies such as isogrid panels for easy fabrication of lightweight satellite structures, CubeSat electronics for standardization of interfaces, STACER antennas for reliable payload antenna deployment, a VLF transmitter capable of tuning to match the LEO plasma environment, and a low-noise VLF receiver.

In conclusion, TERSat will evaluate how efficiently VLF waves can be radiated and propagate in the LEO plasma environment, and enable future missions to explore VLF wave propagation as a method of radiation remediation by answering important questions about the efficiency of interactions of radio waves and high energy particles in the plasma environment of Earth's Van Allen radiation belts at LEO altitudes.

## Acknowledgments

The TERSat program is funded by the AFRL UNP program and by JPL. Graduate student study related to TERSat has been funded in part by the MIT Lincoln Laboratory Scholars program. Undergraduate study has been funded in part by the Massachusetts Space Grant and by the MIT Undergraduate Research Opportunities Program.

The authors would like to acknowledge the work of all of the students on the TERSat program. Additionally, the authors would like to acknowledge the invaluable advice of Prof. David Miller, Paul Bauer, Dr. Alvar Saenz-Otero, Dr. Ivan Linscott, Danilo Roascio, Dr. Greg Ginet, Dr. Michel Ingam, Elizabeth Deems, David Seal, Dr. Ira Katz, Dr. Dan Goebel, Dr. Michael Lisano, Dr. Bodo Reinisch, Dr. Anthea Coster, Dr. Phillip Erickson, Dr. John Foster, Dr. Ethan Miller, Dr. David Voss, and the AFRL UNP staff.

## References

1. B. Abel and R. M. Thorne. "Electron scattering loss in earth's inner magnetosphere I. Dominant physical processes." *Journal of Geophysical Research*, 103(A2):2385–2396, 1998.
2. Air Force Research Lab. University Nanosatellite Program. "Nanosat-7 Users Guide, University Nanosat-7 Program." Kirtland AFB, NM: University Nanosat Program, 2011. Print.
3. J. M. Albert. "Gyroresonant interactions of radiation belt particles with a monochromatic electromagnetic wave." *Journal of Geophysical Research*, 105(A9):21191–21209, 2000.
4. J. M. Albert. "Nonlinear interaction of outer zone electrons with VLF waves." *Geophys. Res. Lett.*, 29(8), 04 2002.
5. AMTEK. "STACER: Spiral Tube and Actuator for Controlled Extension/Retention." Sellersville, PA: AMTEK. Print.
6. K. Balmain. "The impedance of a short dipole antenna in a magnetoplasma." *IEEE Transactions on Antennas and Propagation*, 12(5):605–617, September 1964.
7. Bennett, M., Knight, R., Rasmussen, R., Ingham, M., "State-Based Models for Planning and Execution", ICAPS, 2005. pp. 20-29
8. J. Bortnik, U. S. Inan, and T. F. Bell. "L dependence of energetic electron precipitation driven by magnetospherically reflecting whistler waves." *Journal of Geophysical Research*, 109(A8): 1150, 10.1029/2001JA000303, 2002
9. "CubeSat Kit Motherboard (MB) Hardware Revision E." Pumpkin, Inc, Mar. 2012. Web. May 2012. <[http://www.cubesatkit.com/docs/datasheet/DS\\_CSK\\_MB\\_710-00484-E.pdf](http://www.cubesatkit.com/docs/datasheet/DS_CSK_MB_710-00484-E.pdf)>.
10. "CubeSat Kit Pluggable Processor Module (PPM) D1 Hardware Revision: A." Pumpkin, Inc, Mar. 2012. Web. May 2012. <[http://www.cubesatkit.com/docs/datasheet/DS\\_CSK\\_PPM\\_D1\\_710-00527-A.pdf](http://www.cubesatkit.com/docs/datasheet/DS_CSK_PPM_D1_710-00527-A.pdf)>.
11. Fant, J.S.; Gomaa, H.; Pettit, R.G., "Architectural Design Patterns for Flight Software" 2011 14th IEEE International Symposium on Object/Component/Service-Oriented Real-Time Distributed Computing Workshops (ISORCW), 2011, pp. 97 – 101
12. G. P. Ginet, J. Stuart, A. Adler, D. Smith, M. Scherbarth, et al. "AFRL's Demonstration and Science Experiments (DSX) Mission." In *Proceedings of SPIE*, 2009.
13. J. Haselgrove. "Ray theory and a new method for ray tracing." In *Physics of the Ionosphere*, Volume 1, page 355, 1955.

14. R. A. Helliwell. "Whistlers and related ionospheric phenomena." Stanford University Press Stanford, 1965.
15. R. B. Horne and R. M. Thorne. "Potential waves for relativistic electron scattering and stochastic acceleration during magnetic storms." *Geophysical Research Letter*, 25(15):3011–3014, 1998.
16. U. S. Inan and T. F. Bell. "Pitch angle scattering of energetic particles by oblique whistler waves." *Geophysical Research Letters*, 18:49–52, 1991.
17. U. S. Inan, T. F. Bell, and R. A. Helliwell. "Nonlinear pitch angle scattering of energetic electrons by coherent VLF waves in the magnetosphere." *Journal of Geophysical Research*, 83(A7):3235–3253, 1978.
18. U. S. Inan, H. C. Chang, and R. A. Helliwell. "Electron precipitation zones around major ground based VLF signal sources." *Journal of Geophysical Research*, 89(A5):2891–2906, May 1984.
19. P. Kulkarni, U. S. Inan, and T. F. Bell. "Energetic electron precipitation induced by space based VLF transmitters." *Journal of Geophysical Research*, 113, 2008.
20. McClellan, J., "MotherCube Payload-Telemetry Subsystem Design, Requirements, IDC." 2011. Aurora Flight Sciences MotherCube Program. 7 Dec. 2011.
21. McDonnell-Douglas Astronautics Company, "Isogrid Design Handbook." Prepared for NASA Marshall Spaceflight Center, CR-124075. 1973.
22. B. Mossawir, I. Linscott, et al. "A TID and SEE Radiation-Hardened, Wideband, Low-Noise Amplifier." *IEEE Transactions on Nuclear Science*, Vol. 53, No.6. 2006.
23. B. Reinisch. Personal communication, April 3, 2012.
24. J. Schoenberg, G. Ginet, B. Dichter, M. Xapsos, A. Adler, M. Scherbarth, D. Smith. "The Demonstration and Science Experiments (DSX): A Fundamental Science Research Mission Advancing Technologies that Enable MEO Spaceflight." *Small Satellite System and Services Conference*, 2006
25. P. Song, B. W. Reinisch, V. Paznukhov, G. Sales, D. Cooke, J.-N. Tu, X. Huang, K. Bibl, and I. Galkin, "High-voltage antenna-plasma interaction in whistler wave transmission: Plasma sheath effects." *J. Geophys. Res.*, 112(A3), A03205, [doi:10.1029/2006JA011683](https://doi.org/10.1029/2006JA011683), 2007.
26. R. M. Thorne and C. F. Kennel. "Quasi-trapped vlf propagation in the outer magnetosphere." *Journal of Geophysical Research*, 72(3):857–870, 1967.
27. R. M. Thorne and R.B. Horne. "Landau damping of magnetospherically reflected whistlers." *Journal of Geophysical Research*, 99(A9):17249–17, 1994.
28. A. L. Vampola. "VLF transmission induced slot electron precipitation." *Geophysical Research Letters*, 4(12):569–572, 1977.